TOWARD THE CHARACTERIZATION OF MICRO VORTEX GENERATORS EFFECTS ON SHOCK WAVE/TURBULENT BOUNDARY LAYER INTERACTION USING LES

A. Grébert[1], *J. Bodart*[1], *S. Jamme*[1] *and L. Joly*[1]

[1] *Université de Toulouse, ISAE-Supaéro, DAEP, Département d'Aérodynamique, Énergétique et Propulsion, Toulouse, France*

arnaud.grebert@isae.fr

Abstract

We perform Large Eddy Simulations (LES) of the experimental configuration by Wang et al. (2012): a rake of microramp vortex generators (MVGs) were inserted upstream the SWTBLI. The configuration features MVGs protruding by 0.47δ in a TBL at $M = 2.7$ and $Re_\theta = 3600$. We first validate the flow solver and LES strategy on a baseline configuration without control and we retrieve the characteristic length scales and the low frequency motion ($St_L \approx 0.03$) of the reflected shock foot. The configuration with MVGs exhibits successive regions alternating between either momentum deficit or momentum excess downstream the MVGs, with good agreement with the experiments. Classical wake recovery laws were retrieved as well as the frequency of $St = 0.53$ characteristic of the shedding of intermittent structures downstream the MVGs and we observe a significant 20% decrease of the separation bubble length.

1 Introduction

The shock wave/turbulent boundary layer interaction (SWTBLI) occurs in a wide range of supersonic internal and external flows and has been widely investigated over the last 70 years (see Clemens and Narayanaswamy (2014) for a review).

Among the different possible configurations, the case of an incident oblique shock wave impinging on a flat plate turbulent boundary layer (TBL) is a canonical situation offering a simple framework for understanding the SWTBLI but also frequently encountered in high-speed flows of practical interest. When triggered by a strong SWTBLI at large upstream Mach numbers, the unsteady behaviour of the TBL separation bubble, varying in position and streamwise extent, comes with a low frequency streamwise motion of the reflected shock position just upstream the interaction, with fluctuating pressure and thermal loads as undesirable consequences for the application. This unsteady motion of the region including the reflected shock and the separation bubble, exhibits a wide range of frequencies that have been either correlated to the broad-band perturbations found in the incoming upstream TBL or to a large scale oscillation at much lower frequencies. No consensus about the origin of this low-frequency oscillation has emerged yet, despite the numerous experimental studies that have been conducted to understand and control this unsteadiness. However, recent studies involving Particle Image Velocimetry (PIV) and Direct or Large Eddy Simulations (DNS, LES) allowed to gain deeper insight about the unsteadiness of the interaction, Aubard et al. (2013), and lead to the emergence of two different physical scenarios. Piponniau et al. (2009) advocated a local mass budget of the separated region to link the low-frequency pressure fluctuation to the shear layer developing along the separation line. On the other hand, Touber and Sandham (2011) suggest to consider the boundary layer coupled with the reflected shock as a dynamical system and to interpret the low-frequency motion as is its selective response to a random forcing.

Besides, flow control methods have been proposed to alleviate the SWTBLI-induced impact on performances. Quite recently, micro vortex generators (MVGs) of size typically smaller than the BL thickness have drawn a particular interest as they provide the efficiency of vortex generators (VGs), in suppressing or delaying separation, while minimizing the byproduct induced drag. MVGs are designed to alter the properties of the incoming TBL by introducing vortices in the near-wall region between 0.1δ and 0.5δ, where δ is the boundary layer thickness. In the context of SWTBLI, there were already applied with the aim to reduce the low-frequency oscillations and the amplitude of wall-pressure fluctuations downstream the interaction. Anderson et al. (2006) conducted RANS simulations to evaluate and optimize a large number of MVG designs in order to minimize the boundary layer transformed form factor H_{tr} downstream of the SWTBLI, that is a proper measure of the recovery rate of the TBL downstream the reattachment point. Several experimental and numerical studies followed and highlighted the distinctive flow features around and downstream the MVGs (see Panaras and Lu (2015) for a review). Despite their simple geometry, the flow

structure and dynamics downstream microramp vortex generators have been recognized to undergo a complex evolution process, leading to different interpretations of the associated flow patterns in the near wall region downstream.

These considerations and still wide-open conjectures motivate the present work that proceeds by LES to *i)* validate the flow solver and LES strategy *ii)* characterize the SWTBLI mean flow properties and unsteady shock dynamics of the present configuration *iii)* gain further insight about the flow structure downstream microramp-type MVGs in order to identify physical mechanisms induced and quantify their influence on the SWTBLI.

2 Flow Solver

The present LES were performed using the massively parallel CharLES^X solver, developed in CTR Stanford, which solves the spatially filtered compressible Navier-Stokes equations for conserved quantities using a finite volume formulation and a control-volume-based discretization on unstructured hexahedral meshes. An explicit third-order Runge-Kutta (RK3) is used for time advancement. It relies on Vreman' subgrid-scale (SGS) model to represent the effect of unresolved small-scale fluid motions. It also features a solution-adaptive methodology which combines a non-dissipative centred numerical scheme and an essentially non-oscillatory (ENO) second-order shock-capturing scheme. The latter is applied in regions around shock waves, identified by a shock sensor sensitized to local dilatation, enstrophy and sound speed (see Bermejo-Moreno et al. (2014), for more details about the numerics). The solver has been successfully used to study confinement effects in SWTBLI, Bermejo-Moreno et al. (2014).

3 Numerical set-up

The configuration selected in the present work strictly follows Wang et al. (2012) experiments, as sketched in figure 1. It is characterized by a freestream Mach number of $M = 2.7$ and a Reynolds number $Re_\theta = 3600$ based on the TBL momentum thickness at the position of impact of the incident shock. As in the experiments, a shock generator is included on the opposite wall yielding a flow deflection of $\phi = 10.5°$.

The grid parameters used for the present LES are given in Table 1. The spanwise extent of the computational domain has been carefully chosen according to previous works by Touber and Sandham (2008) and Bermejo-Moreno et al. (2014), and is aimed at preventing spurious effects on the size of the separation bubble L_{sep}. The spanwise extent of the domain is thus set to $5.75\delta_0$, where δ_0 is the TBL thickness at $0.5L_{sep}$ upstream of the separation bubble, leading to a domain 1.2 times larger than the interaction length scale L_{int}. As a consequence, the spanwise extent of the domain includes two spanwise periods of the MVGs rake in order to replicate the geometry of Wang et al. (2012) experiments.

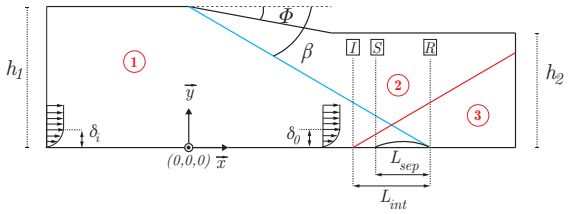

(a)

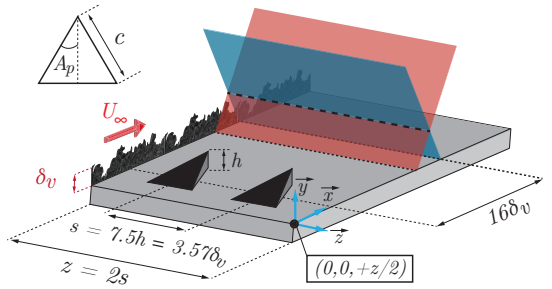

(b)

Figure 1: (a) Reference parameters and length scales. (b) Configuration of the present LES with control devices.

Δx^+	$\Delta y^+_{\min}$	Δz^+	L_x/δ_0	L_y/δ_0	L_z/δ_0
20	1	15	40.15	12.05	5.75

Table 1: Grid parameters for the LES with δ_0 the BL thickness just ahead of the interaction

The microramp geometry is the same as in the experiments with a height of $h = 0.47\delta_v$ (where δ_v is the TBL thickness immediately upstream of the MVG), a chord length $c = 7.2h$ and a wedge half-angle $A_p = 24°$. The grid is refined gradually toward the leading edge and sides of the microramp, with $\Delta x^+ = 7.5$ and $\Delta z^+ = 3$. The two MVGs are located at $16\delta_v$ from the impingement shock incident point and at $23\delta_i$ from the inlet to avoid spurious effect of the inflow condition.

The TBL is established by using the digital filter inlet conditions proposed in Xie and Castro (2008) and modified by Touber and Sandham (2009). The parameters of the digital filter are chosen according to Touber and Sandham (2009) prescription.

Periodic spanwise boundary conditions and symmetry conditions for the shock generator and downstream top part of the computational domain are used.

Two simulations have been carried out on the same computational domain. The first configuration is the baseline one with no control, *i.e.*without any MVG, and the second one features two MVGs with SWTBLI. The first simulation is used to validate the inflow

boundary condition and to characterize the SWTBLI.

4 Shock wave/turbulent boundary layer interaction

Incoming turbulent boundary layer

Prior to addressing the SWTBLI, we assess the restitution of the main properties of the incoming boundary layer. Using the baseline configuration, *i.e.* without MVGs, the spatial development of a supersonic TBL is considered downstream inflow conditions, obtained using the digital filter approach. The van-Driest-transformed mean velocity profile and the RMS of the Reynolds stresses are plotted in Figure 2 and Figure 3. They are compared to the DNS data of Pirozzoli and Bernardini (2013) and Schlatter and Örlü (2010) for an identical Reynolds number $Re_\tau = 499$, corresponding to a location just upstream of the present SWTBLI. The Reynolds stresses are reported using the van-Driest multiplier, semi local scaling, $\xi = \sqrt{\langle\rho\rangle/\rho_w}$, where $\langle\bullet\rangle$ denotes the time averaging and the subscript w refers to quantities at the wall. It should be noted that the DNS of Pirozzoli and Bernardini (2013) has a slightly different Mach number of $M = 3$ and that the DNS of Schlatter and Örlü (2010) is performed for incompressible flow conditions. The velocity profile, Figure 2 is in good agreement with the logarithmic law of the wall and the DNS data, especially with the data from Pirozzoli and Bernardini (2013). The Reynolds normal stresses $\langle u_i' u_i' \rangle$ are in an overall good agreement with DNS data. However, the turbulent shear stress $\langle u'v' \rangle$ is slightly overestimated over the whole TBL.

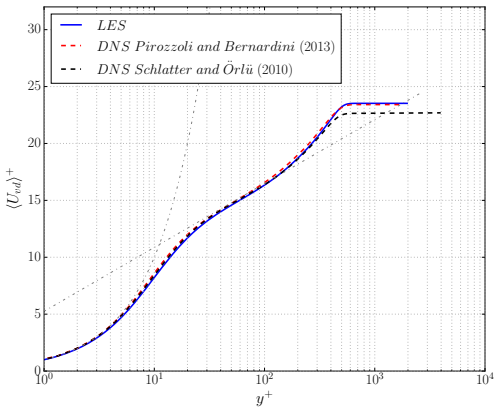

Figure 2: van-Driest transformed mean-velocity profile compared to references at $Re_\tau = 499$.

For further validation, the streamwise evolution of the incompressible skin friction coefficient, obtained using the van-Driest II transformation, is plotted in Figure 4. The time-averaged skin-friction coefficient $\langle C_{f_i} \rangle$ is in very good agreement with the DNS results of Schlatter and Örlü (2010) and the LES results of Eitel-Amor et al. (2014)

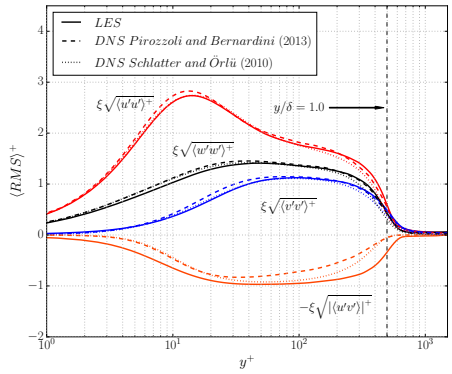

Figure 3: RMS of Reynolds Stresses with density scaling $\xi = \sqrt{\langle\rho\rangle/\rho_w}$ at $Re_\tau = 499$.

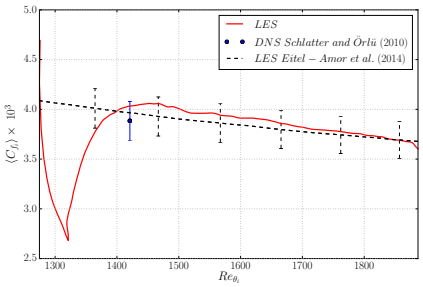

Figure 4: Incompressible skin friction coefficient evolution. Error bars indicates $\pm 5\%$ of value.

SWBTLI

In the region of the interaction with the shock wave, the flow is decelerated due to the correlative adverse pressure gradient imposed on the boundary layer. As a consequence, a separation bubble forms between the incident and reflected shocks where reverse flow conditions are associated with a negative wall shear stress. This is clearly seen from evolution of the mean skin friction coefficient $\langle C_f \rangle$ in the vicinity of the interaction, as shown in Figure 5. The letter S refers to the separation point of the recirculation zone whereas R indicates the reattachment point. The length scale of the separation bubble L_{sep} is simply the distance between S and R. The length scale of the whole interaction region, L_{int} is larger than L_{sep} and is computed using the distance between I and R, see Figure 1, where I is the starting point of the interaction region. The position of I can be measured both by extrapolation of the reflected shock wave towards the wall and by detecting a wall pressure increase by more than 1% of the upstream wall pressure. The measured length scales for the present LES compare very well with literature references given in Table 2 but established at $M = 2.3$ instead of $M = 2.7$, since no measurement of these length scales is available from Wang et al. (2012) experiments.

We now analyze the Power Spectral Densities (PSD) of wall-pressure data to address the unsteadi-

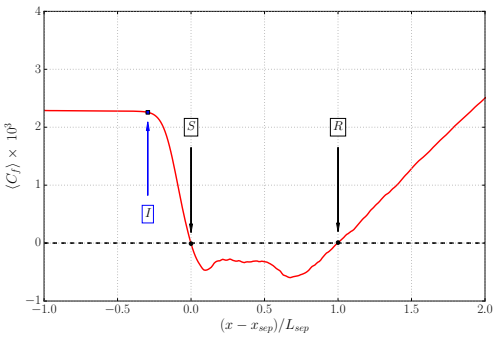

Figure 5: Compressible skin friction evolution. I, S, R denote the beginning of the interaction, the beginning and the end of the separation bubble, respectively.

Case	L_{sep}/δ_0	L_{int}/δ_0	Re_θ
Current LES	3.78	4.89	3600
Aubard et al. (2013)	4.3	4.78	3725
Touber et al. (2009)	3.9	4.8	5100

Table 2: Interaction length scales for the present LES and some references.

ness of the reflected shock dynamics. Pressure signals are recorded using 456 equally spaced probe lines distributed from $x = -9\delta_0$ and $x = 8\delta_0$ around the location of shock impingement, with a streamwise resolution of $\Delta x/\delta_0 = 0.036$. Each probe line, at a given streamwise position, covers the entire spanwise extent of the computational domain with a resolution of $\Delta z/\delta_0 = 0.081$. Pressure data are recorded after an initial transient of $390\delta_0/U_\infty$ with a constant sampling time of $0.01\delta_0/U_\infty$ for a total integration time of $2350\delta_0/U_\infty$. Therefore, the maximum resolvable Strouhal number $St_L = fL_{sep}/U_\infty$ based on the separation length scale is $St_{L_{\max}} = 380$ and a minimum resolvable Strouhal number $St_{L_{\min}} = 1.6\times10^{-3}$ which means that our simulation is able to capture almost 19 low-frequency oscillations at a $St_L = 0.03$ based on the conclusions by Dupont et al. (2006).

The weighted PSD of the wall pressure, presented in Figure 6, normalised by the local wall-pressure variance is obtained using using Welch's method by splitting the signal in 8 segments with 50% overlaps and Hamming windows. A first remark is that no forcing is found in the incoming turbulent boundary layer in the mid and low frequency ranges of interest. This is highlighting that the wall turbulence is clearly independent of the inflow boundary condition. A low-frequency content is found around the separation point and is indeed associated with the low-frequency oscillation of the reflected shock at the expected $St_L = 0.03$. Downstream the interaction zone, a significant spectral content develops up to a Strouhal number of 0.5 and is associated with the thickening of the boundary layer and the shedding of coherent vortices in the shear layer on top of the recirculation bubble.

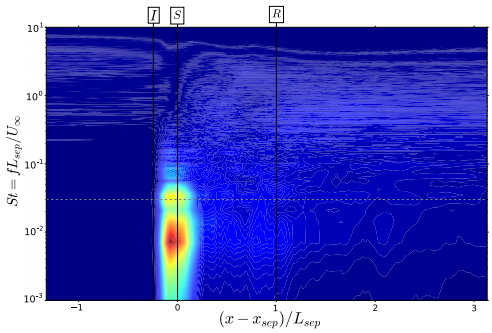

Figure 6: Weighted power spectral density (PSD) of spanwise-averaged wall-pressure signals. Dashed gray line indicates $St_L = 0.03$.

5 Vortex generator

We now set the flow configuration according to the experiments of Wang et al. (2012) by inserting two microramps in the computational domain located at a distance of $16\delta_v$ upstream the impingement point of the incident shock, see Figure 7. Therefore, we are able to characterize the flow organization around and downstream of the microramps, before the interaction zone, with an integration time of 31 flow-through time over the $16\delta_v$ distance between the MVGs and the interaction. To gain insight into the mechanism induced by the microramp, the time-averaged velocity distribution in the spanwise direction is measured at $y = 0.5h$ above the wall. The velocity is reported in the following form $(U - U_L)/U_e$, where U_L is the local velocity in the uncontrolled case and U_e the velocity at the TBL edge. Figure 8 shows the velocity for three different streamwise locations downstream the microramp for the present simulation compared with Wang et al. (2012) measurements. An overall good agreement is obtained with the experimental data and we retrieve the expected streamwise momentum deficit behind each microramp, especially at the location $x = 6.7h$. The velocity defect is rapidly cancelled, but the mean velocity remains below the one of the uncontrolled case while two velocity excess are found on each side of the median plane of both microramps. Finally, for downstream distances as large as $x = 13.3h$ and $x = 20h$, another streamwise momentum deficit is seen to form gradually at mid spanwise distance between the MVGs, with levels as low as those found in their wake.

To characterize more precisely the wake recovery, the streamwise time-averaged velocity field is studied by extracting the maximum velocity deficit $U_{\min}$ in the median plane of each MVG, from $x = 12h$ to $x = 32h$ downstream of the microramp. The wall-normal velocity field is studied in a similar way by extracting the maximum wall-normal velocity $V_{\max}$ in order to characterize the upwash induced by the microramp. Figure 9 displays the streamwise evolution of

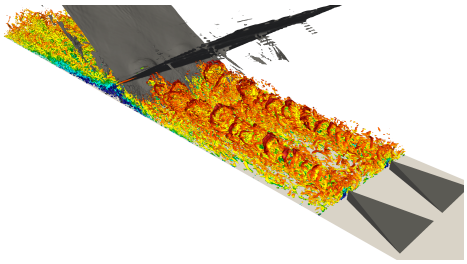

Figure 7: Instantaneous visualization of the turbulent structures and shock waves downstream the MVGs using Q criterion and iso-surface of dilatation, respectively.

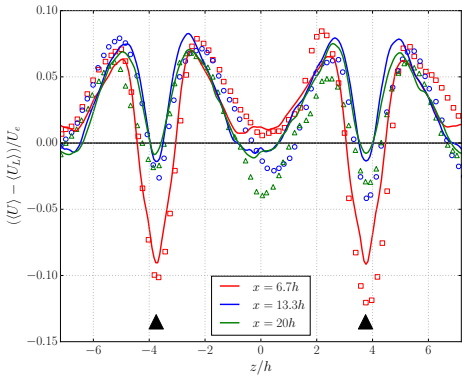

Figure 8: Averaged velocity differences in the wake of the microramp at $y = 0.5h$ for different streamwise distance downstream of the MVG. Symbols represent the measurement performed by Wang et al. (2012). Black triangles denote the MVGs location.

the wake and upwash recovery as well as a power-law fit for each quantity. We retrieve the power-law evolution of the wake recovery with an exponent of 0.83, slightly higher than the value of 0.75 predicted by the theory and the one retrieved by Sun et al. (2014). As mentioned by the latter, the difference is ascribed to the presence of boundary layer turbulence providing additional mixing, which is even more pronounced in our simulation since the Mach number of the upstream flow is higher in our case than in Sun et al. (2014) ($M = 2.0$). Moreover, the value obtained for the fitted exponent of the upwash velocity decay (1.98) is 2.4 times the one calculated for the velocity deficit, which is in agreement with the ratio between the two quantities reported by Sun et al. (2014).

As shown in Figure 7, a complex instantaneous flow field organization can be observed downstream of the MVGs where the shedding of large scale hairpin vortices seems to emerge. This phenomenon has already been reported in Wang et al. (2012) and Sun et al. (2014), and it will certainly have an impact on the SWTBLI characteristics. A typical spatial period of the coherent structures can be estimated thanks to the autocorrelation function of 4 different scalar fields: density ρ, temperature T, pressure P and the spanwise vorticity ω_z. Figure 10 shows these autocorrelation functions calculated in a rectangular region in the median plane downstream of the microramp between $x = 10\delta_v - 14\delta_v$ and $y = 0.5\delta_v - 2.5\delta_v$.

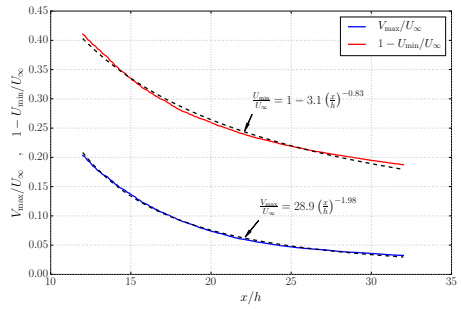

Figure 9: Streamwise decay evolution of maximum upwash velocity $V_{\max}/U_\infty$ and velocity difference between wake core and freestream.

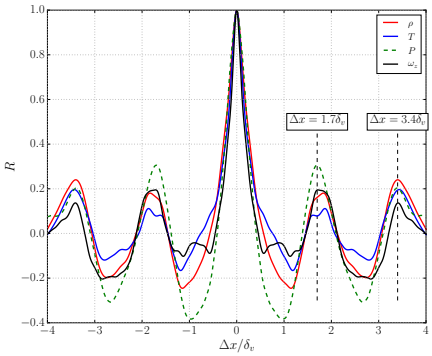

Figure 10: Autocorrelation of the large-scale structure in the median plane inside the wake at location $x = 10\delta_v - 14\delta_v$ downstream of the MVG.

Several peaks can clearly be observed on the autocorrelation functions for all scalar fields. The distance between the first and second peak ($\Delta x/\delta_v = 1.7$) can be interpreted as a dominant spatial period for the coherent structures observed in the region of the wake where the functions are calculated. By considering an average convection velocity in this region, taking into account the aforementioned velocity deficit $U_{deficit} = 0.9U_e$, a non-dimensional frequency of $St = f\delta_v/U_e \approx 0.53$ can be extracted for these coherent structures. This value is similar to the one exhibited by Sun et al. (2014), Wang et al. (2015) and is in the range of the frequency observed in the experiments of Wang et al. (2012). Finally, we observe a significant decrease of the separation bubble length, under the control of MVGs, with an averaged value of $L_{sep} = 3.19\delta_0$, where δ_0 the TBL thickness of the uncontrolled case.

6 Conclusions

In this work, high fidelity LES have been con-

ducted in order to address the control of the shock wave/turbulent boundary layer interaction configuration using microramp vortex generators. The numerical approach has first been validated by considering the SWTBLI problem alone without any control devices. This allowed to assess both the quality of the incoming turbulent boundary layer and the physics of the SWTBLI in terms of characteristic frequencies ($St_L = 0.03$) and interaction length scales. A second simulation including the MVGs upstream of the interaction system could then be conducted, based on Wang et al. (2012) experiments. The study of the flow downstream of the microramps showed good agreement with the reference experiments and previous LES of the same flow configuration (Sun et al. (2014)). The alternating momentum deficits and high speed regions in the wake of the MVGs were correctly reproduced. The good wake recovery laws were also obtained, as well as the typical frequency of $St = 0.53$ corresponding to the shedding of intermittent structures downstream of the microramps. The effect of the MVGs on the SWTBLI could then be investigated with confidence and showed a great capability of these control devices to reduce the interaction length. Further investigation in the frequency domain are now under progress in order to characterize the MVGs' influence on the low frequency shock foot motion.

Acknowledgments

This research was supported in part by the French Ministry of Defence through a financial support of the DGA. Authors would like to thank the continuous support and computational resources provided by CNRS on Turing and Occigen (GENCI-IDRIS and GENCI-CINES, Grant x20162a7178), Eos (CALMIP, Grant 2016-p1425).

References

Anderson, B. H., Tinapple, J., and Surber, L., (2006). Optimal Control of Shock Wave Turbulent Boundary Layer Interactions Using Micro-Array Actuation. *AIAA paper*, Vol. 3197, No. June, pp. 1–14.

Aubard, G., Gloerfelt, X., and Robinet, J.-C., (2013). Large-Eddy Simulation of Broadband Unsteadiness in a Shock/Boundary-Layer Interaction. *AIAA Journal*, Vol. 51, No. 10, pp. 2395–2409.

Bermejo-Moreno, I., Campo, L., Larsson, J., Bodart, J., Helmer, D., and Eaton, J. K., (2014). Confinement effects in shock wave/turbulent boundary layer interactions through wall-modelled large-eddy simulations. *Journal of Fluid Mechanics*, Vol. 758, pp. 5–62.

Clemens, N. T. and Narayanaswamy, V., (2014). Low-Frequency Unsteadiness of Shock Wave/Turbulent Boundary Layer Interactions. *Annual Review of Fluid Mechanics*, Vol. 46, No. September, pp. 469–492.

Dupont, P., Haddad, C., and Debiève, J.-F., (2006). Space and time organization in a shock-induced separated boundary layer. *Journal of Fluid Mechanics*, Vol. 559, pp. 255.

Eitel-Amor, G., Örlü, R., and Schlatter, P., (2014). Simulation and validation of a spatially evolving turbulent boundary layer up to Re_θ 8300. *International Journal of Heat and Fluid Flow*, Vol. 47, pp. 57–69.

Panaras, A. G. and Lu, F. K., (2015). Micro-vortex generators for shock wave/boundary layer interactions. *Progress in Aerospace Sciences*, Vol. 74, pp. 16–47.

Piponniau, S., Dussauge, J. P., Debiève, J.-F., and Dupont, P., (2009). A simple model for low-frequency unsteadiness in shock-induced separation. *Journal of Fluid Mechanics*, Vol. 629, pp. 87.

Pirozzoli, S. and Bernardini, M., (2013). Probing high-Reynolds-number effects in numerical boundary layers. *Physics of Fluids*, Vol. 25, No. 2.

Schlatter, P. and Örlü, R., (2010). Assessment of direct numerical simulation data of turbulent boundary layers. *Journal of Fluid Mechanics*, Vol. 659, pp. 116–126.

Sun, Z., Schrijer, F. F. J., Scarano, F., and van Oudheusden, B. W., (2014). Decay of the supersonic turbulent wakes from micro-ramps. *Physics of Fluids*, Vol. 26, No. 2, pp. 025115.

Touber, E. and Sandham, N. D., (2008). Oblique Shock Impinging on a Turbulent Boundary Layer: Low-Frequency Mechanisms. *AIAA paper*, Vol. 4170.

Touber, E. and Sandham, N. D., (2009). Large-eddy simulation of low-frequency unsteadiness in a turbulent shock-induced separation bubble. *Theoretical and Computational Fluid Dynamics*, Vol. 23, No. 2, pp. 79–107.

Touber, E. and Sandham, N. D., (2011). Low-order stochastic modelling of low-frequency motions in reflected shock-wave/boundary-layer interactions. *Journal of Fluid Mechanics*, Vol. 671, pp. 417–465.

Wang, B., Liu, W., Zhao, Y., Fan, X., and Wang, C., (2012). Experimental investigation of the microramp based shock wave and turbulent boundary layer interaction control. *Physics of Fluids*, Vol. 24, No. 5, pp. 055110.

Wang, B., Liu, W. D., Sun, M. B., and Zhao, Y. X., (2015). Fluid Redistribution in the Turbulent Boundary Layer Under the Microramp Control. *AIAA Journal*, Vol. 53, No. 12, pp. 3777–3787.